Journal of Fluids and Structures (2000) **14,** 221–234
doi:10.1006/jfls.1999.0258, available online at http://www.idealibrary.com on IDEAL®

A FLUID–STRUCTURE MODEL FOR FAST BRITTLE FRACTURE IN PLASTIC PIPES

C. J. Greenshields†, G. P. Venizelos and A. Ivankovic

Department of Mechanical Engineering, Imperial College of Science, Technology and Medicine, Exhibition Road, London SW7 2BX, U.K.

(Received 4 November 1998 and in revised form 1 June 1999)

This paper presents an intermediate stage in the development of a unified computational model based on finite volume (FV) discretization, for coupled fluid–structure analysis of rapid crack propagation fluid-pressurized plastic pipes. The pressure profile behind the crack tip, which is the main source of the crack driving force, is computed by combining a one-dimensional (1-D) gas flow analysis with FV stress analysis of the pipe. The coupled model is then validated against experimental results and used to determine the dependence of crack driving force on crack speed and to study the effect of various physical parameters on crack driving force.

1. INTRODUCTION

Over 30 years ago, fast brittle fracture was identified as an inherently catastrophic failure mode in plastic gas pipelines. Although fast cracks seemed difficult to initiate, subsequent rapid crack propagation (RCP) was thought to be possible at pressures lower than the rated pressure, imposed by design against slow crack growth. Rapid escape of compressed gas during such a failure could cause severe structural damage to roads and pavements above the pipeline; the possibility of a fuel gas explosion increases the overall destructive potential. RCP is characterized by long cracks extending axially at high speed (typically exceeding 100 m/s) and the conditions under which it can occur are well defined: a critical pressure exists above which the crack can propagate indefinitely, and below which it will promptly arrest. A crack might be initiated from a defective butt fusion weld joint or an external impact from a "third party" and no amount of care can completely eliminate the risk. The study of RCP in gas pipes therefore aims to ensure that a fast-running crack will always arrest, even under the most extreme operating conditions.

In the early 1970s, British Gas responded quickly to minimize the risk of RCP failure in polyethylene (PE) gas pipelines. The central part of their effort has been the development of a full-scale test (ISO 13478, 1996). The results of early experiments gave an invaluable insight into the problem but the preparation time and cost of each test inevitably has made progress slow. In 1987, Imperial College began to develop a laboratory test to reproduce the full-scale RCP phenomenon in short, manageable pipe specimens. The small-scale steady-state (S4) test was quickly developed to the point where the RCP phenomenon could be reproduced reliably within a laboratory to assess the performance of different materials. The principal drawback of the method is that critical pressures measured by the S4 test are lower than their full-scale equivalents, typically by a factor of 5 (Greig 1996).

† Present address: Department of Mechanical Engineering, King's College, Strand, London WC 2R 2LS, U.K.

0889–9746/00/020221 + 14 $35.00/0

Despite the rarity of RCP failures, there is little room for complacency, since the gas companies need to exploit the commercial advantages of larger diameter pipes operating at higher pressures and the pipe/polymer manufacturers are introducing new products at an ever increasing rate. Present technology can be used to assess these products with reasonable confidence but if it were possible to predict safe (i.e., full-scale) operating pressures from S4 performance, development costs would be significantly reduced. This cannot be realistically achieved without an adequate coupled fluid–structure–fracture model and since the problem is so complex, a numerical approach is the only credible one. O'Donoghue *et al.* (1991) have previously used the finite element method in a fluid–structure model to investigate fracture propagation in steel pipelines. Ivankovic *et al.* (1997) and Ivankovic & Venizelos (1997, 1998) have more recently demonstrated that the finite volume (FV) method can adequately solve the stress analysis and fracture components of pipe RCP. In that work the fluid was represented by fixed pressure tractions along the bore of the pipe; the goal is obviously to develop a fully coupled fluid–structure numerical procedure for tackling the problem. In this paper, we present an intermediate model for the S4 test, where we have coupled our finite volume code with a 1-D gas flow analysis.

2. THE S4 TEST

The S4 test is the preferred choice for research and material development because it closely simulates full-scale conditions, but at lower cost and in the comfort of a laboratory (ISO 13477, 1996). The method uses a pipe specimen, seven diameters in length, which is sealed at both ends and pressurized with air (Figure 1). A sharp chisel-ended striker, impacts the pipe near one end and drives a fast running crack into the main test section of the pipe. While the crack propagates along the pipe, axial decompression ahead of the crack tip is suppressed by means of internal disc baffles, spaced along the pipe length. The crack has only to travel a short distance before it experiences steady-state conditions which are characteristic of a fully developed crack propagation in the full-scale test. If the crack driving force is too small to overcome the fracture resistance of the material, the crack promptly arrests; with a sufficiently high driving force, the pipe "unzips" fully along its length. A containment cage restricts spurious crack arrest at supercritical pressures when excess flaring of the pipe walls can cause rapid decompression and a sudden loss of crack driving force. It should be noted

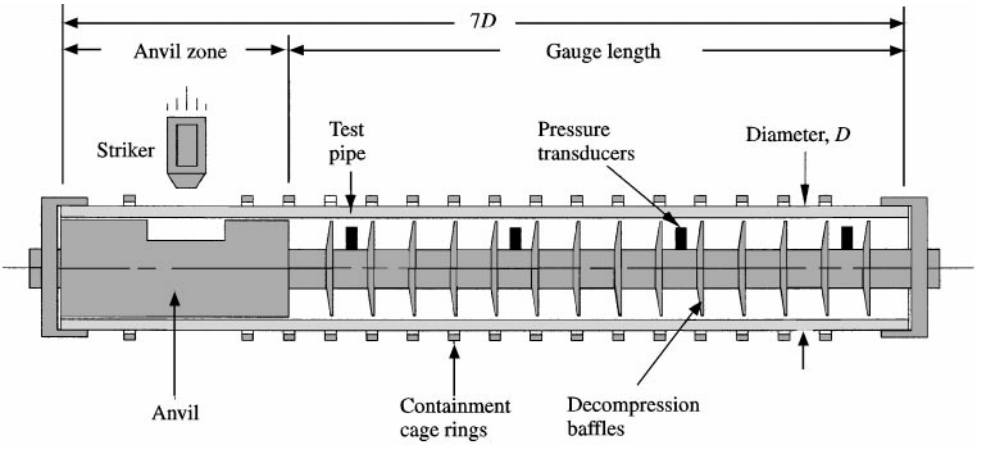

Figure 1. Schematic diagram of S4 test apparatus.

that the discrepancy between S4 and full-scale critical pressure is primarily caused by the restriction on axial motion of the fluid imposed by the internal baffles.

3. FINITE VOLUME MODEL

This section briefly outlines the FV method, when applied to the analysis of RCP in plastic pipes. This is a small strains formulation, and therefore no distinction is made between deformed and undeformed configurations.

3.1. Mathematical Formulation

The incremental form of conservation of linear momentum, used for the analysis of a nonlinear elastic material, can be expressed as

$$\frac{\partial}{\partial t}\int_V \rho \frac{\partial(\delta \mathbf{u})}{\partial t}\,\mathrm{d}V = \int_S \delta\boldsymbol{\sigma}\cdot\mathbf{n}\,\mathrm{d}S + \int_V \rho\,\delta\mathbf{f}\,\mathrm{d}V. \tag{1}$$

Here, V is the volume of the body bounded by a surface S, with the unit vector normal $\mathbf{n}$ pointing outwards, ρ is the mass density, $\mathbf{u}$ is the displacement vector, $\boldsymbol{\sigma}$ is the symmetric stress tensor, and $\mathbf{f}$ is the body force. Displacement, stress and body force increments are denoted as $\delta\mathbf{u}$, $\delta\boldsymbol{\sigma}$ and $\delta\mathbf{f}$, respectively.

Temperature effects are not accounted for and the behaviour of nonlinear elastic pipe materials such as medium density polyethylene (PE80) is described by an incremental Hooke's law,

$$\delta\boldsymbol{\sigma} = 2\mu\delta\boldsymbol{\varepsilon} + \lambda\,\mathrm{div}\,\delta\mathbf{u}\mathbf{I}, \tag{2}$$

where μ and λ are Lamé's coefficients, $\mathbf{I}$ is the identity tensor, and the increments of the strain tensor $\boldsymbol{\varepsilon}$ are defined as

$$\delta\boldsymbol{\varepsilon} = \tfrac{1}{2}[\mathrm{grad}\,\delta\mathbf{u} + (\mathrm{grad}\,\delta\mathbf{u})^{\mathrm{T}}]. \tag{3}$$

Combining equations (1)–(3) and neglecting body forces gives the following equation in terms of unknown displacement vector increments:

$$\frac{\partial}{\partial t}\int_V \rho \frac{\partial(\delta \mathbf{u})}{\partial t}\,\mathrm{d}V = \int_S \{\mu[\mathrm{grad}\,\delta\mathbf{u} + (\mathrm{grad}\,\delta\mathbf{u})^{\mathrm{T}}] + \lambda\,\mathrm{div}\,\delta\mathbf{u}\mathbf{I}]\}\cdot\mathbf{n}\,\mathrm{d}S. \tag{4}$$

3.2. Solution Method

A coordinate system has to be chosen in order to discretize equation (4). Although components of vectors and tensors related to a global Cartesian system are generally preferred, since they lead to a strongly conservative form of the momentum equation, a cylindrical coordinate system (θ, r, z) is chosen here because of the specific geometry of the problem. The solution domain (Figure 2) is divided into a number of contiguous cylindrical control volumes, or cells, with six cell faces S_k $(k = 1, \ldots, 6)$. The time domain is subdivided into a number of arbitrary time steps δt. The computational nodes are placed at the centres of the control volumes, while the boundary nodes, required for the specification of boundary conditions, at the centres of the boundary cell faces. Dependent variables and material

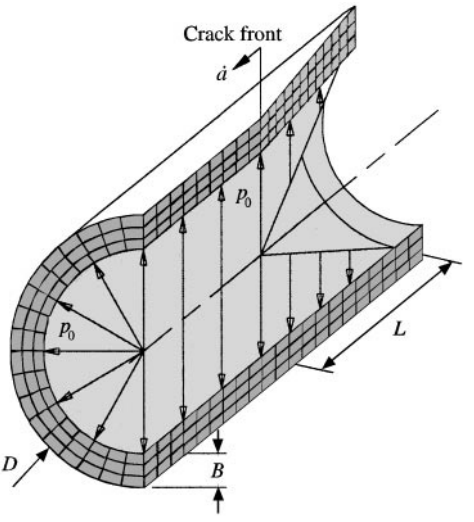

Figure 2. Pipe solution domain; D is the pipe outer diameter, B the pipe wall thickness, $\dot{a}$ the crack speed, p_0 the crack tip pressure, and L is the decompression length.

properties are stored in the computational nodes. When equation (4) is applied to an arbitrary cell containing centre point P_0, it takes the form

$$\frac{\partial}{\partial t}\int_{V_{P_0}} \rho \frac{\partial(\delta\mathbf{u})}{\partial t}\,\mathrm{d}V = \sum_{k=1}^{6}\int_{S_k} \{\mu[\operatorname{grad}\delta\mathbf{u} + (\operatorname{grad}\delta\mathbf{u})^{\mathrm{T}}] + \lambda \operatorname{div}\delta\mathbf{u}\mathbf{I}\}\cdot\mathbf{n}\,\mathrm{d}S. \tag{5}$$

In order to solve equation (5), the exact integrals have to be approximated, and a distribution of dependent variables and physical properties in space and time has to be assumed. In the FV procedure adopted, both surface and volume integrals are calculated employing the mid-point rule. For example, the volume integrals is approximated as

$$\int_{V_{P_0}} \rho \frac{\partial(\delta\mathbf{u})}{\partial t}\,\mathrm{d}V \approx \rho\left(\frac{\partial(\delta\mathbf{u})}{\partial t}\right)_{P_0} V_{P_0}, \tag{6}$$

where the term in brackets has the value at the cell centre P_0, and V_{P_0} is the cell volume. A linear spatial distribution of displacement increments is employed. Both approximations are second-order-accurate. Physical properties at the cell faces are obtained by harmonic interpolation. For temporal variation of dependent variables, a fully implicit time discretization is adopted because of its unconditional stability. All dependent variables are expressed in the current time step δt^m, except in the transient term, in which a two-time-level linear variation with time of the deformation velocity increment is adopted:

$$\frac{\partial}{\partial t}\int_{V_{P_0}} \rho \frac{\partial(\delta\mathbf{u})}{\partial t}\,\mathrm{d}V \approx \frac{\rho V_{P_0}}{\delta t^m}\left[\left(\frac{\delta\mathbf{u}^m - \delta\mathbf{u}^{m-1}}{\delta t^m}\right)_{P_0} - \left(\frac{\delta\mathbf{u}^{m-1} - \delta\mathbf{u}^{m-2}}{\delta t^{m-1}}\right)_{P_0}\right]. \tag{7}$$

The magnitude of the time-step is restricted only by the temporal accuracy requirement and the simulations in this work are too rapid to suffer from effects of numerical damping associated with the time integration procedure used. Initial conditions, in terms of initial increments of displacements and velocities are required to start the calculation. Boundary

conditions are implemented by substituting traction or displacement increments on the boundary cell faces in equation (5) with prescribed values.

Now, equation (5) can be represented by the following algebraic equation which relates displacement increment vector $\delta\mathbf{u}_{P_0}$ at the centre of the cell with those of neighbouring cells $\delta\mathbf{u}_{P_k}$:

$$a_{P_0}\delta\mathbf{u}_{P_0}^m - \sum_{k=1}^{6} a_k \delta\mathbf{u}_{P_k}^m = \mathbf{b}_{P_0}, \quad a_{P_0} = \sum_{k=1}^{6} a_k + \frac{\rho V_{P_0}}{(\delta t^m)^2}. \tag{8}$$

The coefficients a_k and the source term $\mathbf{b}_{P_0}$ are functions of geometry and material properties, with b_{P_0} also containing some unknown dependent variables. As a result of FV discretization, three mutually coupled sets of N nonlinear algebraic equations with three unknown displacement increment components (δu_θ, δu_r, δu_z) are obtained, where N is the number of cells. A segregated solution procedure is employed to solve these equations; sets of equations for each dependent variable are temporarily decoupled by assuming that coefficients and the right-hand side of equation (8) are known—calculated using an initial guess or dependent variable values from the previous iteration. Consequently, a system of linear algebraic equations is obtained for each displacement increment component in the form

$$A\delta\mathbf{u} = \mathbf{b}, \tag{9}$$

where A is a seven-diagonal, diagonally dominant, positive-definite, symmetric, sparse $N \times N$ matrix. Vector $\delta\mathbf{u}$ contains values of current displacement increment vector components, and $\mathbf{b}$ accommodates sources at N nodes. The segregated solution approach enables reuse of the same storage for A and $\mathbf{b}$ for all $\delta\mathbf{u}$ components, resulting in very small computer memory requirements—only $8N$ storage locations are required: $7N$ for matrix A and N for vector $\mathbf{b}$. Equation (9) is solved sequentially in turn for each $\delta\mathbf{u}$ component using a line-by-line TDMA iterative solver adapted for solving seven-diagonal systems, which takes advantage of the structured mesh employed in this study. There is no need to solve equation (9) to a tight tolerance since A and $\mathbf{b}$ are only approximations, based on the solution from the previous iteration, and reduction of residuals by one order of magnitude is normally sufficient. After solving equation (9) for all three components of displacement increments, elements of coefficient matrix A and $\mathbf{b}$ are updated and the procedure is repeated until overall convergence is reached, i.e., the sum of absolute residuals for all equations has fallen below a prescribed tolerance. In order to promote stability of the solution method, an under-relaxation procedure is sometimes necessary.

Having calculated displacement increments, stress increments are obtained from equation (2). The total displacements and stresses in the current time-step are calculated as

$$\mathbf{u}^m = \mathbf{u}^{m-1} + \delta\mathbf{u}^m, \qquad \boldsymbol{\sigma}^m = \boldsymbol{\sigma}^{m-1} + \delta\boldsymbol{\sigma}^m, \tag{10}$$

respectively. The solution is then advanced to the next time-step, where the whole procedure is repeated.

3.3. Transient Crack Propagation

The conventional *holding back force technique*, discussed in Nishioka (1997), is employed for the analysis of a straight crack propagating rapidly along the pipe. Due to symmetry, only half of the pipe is modelled. First, the solution is obtained for the quasi-static loading of the uncracked pipe by a uniformly applied pressure p_0, which provides initial conditions for the transient calculation. A planar crack is advanced from the point of initiation according to

a specified crack length history by successive release of rows of cells aligned in the radial direction. Surface forces on the released cell faces are decayed linearly from their maximum values at the instant of release to zero as the crack traverses the cell face. The energy absorbed by the propagating crack—the crack driving force G—is then calculated from the work done by these local forces:

$$G = \sum_{i=1}^{N_t} \left(\frac{\mathrm{d}W_h}{\mathrm{d}A} \right)_i = \frac{2}{B\mathrm{d}a} \sum_{i=1}^{N_t} \left(\int_0^{u_c} F_h \, \mathrm{d}u_c \right) \approx \frac{2}{B\delta z} \sum_{i=1}^{N_t} \sum_{t_p}^{t_n} [F_h^m (u_c^m - u_c^{m-1})]_i. \tag{12}$$

where $(W_h)_i$ is the work done by the holding back force $(F_h)_i$ acting on the released cell face i, $\mathrm{d}A = B\,\mathrm{d}a$ is the fracture surface created upon an increment $\mathrm{d}a$ of crack growth cross a wall thickness B, δz is the axial length of the crack tip cells, N_t is the number of cells through the thickness, u_c is half of the crack tip opening displacement, and t_p and t_n are the release times of the present and future crack front cells. The accuracy of the solution can be compared with the global energy balance approach:

$$G = \frac{\mathrm{d}W_e}{\mathrm{d}A} - \frac{\mathrm{d}E_s}{\mathrm{d}A} - \frac{\mathrm{d}E_k}{\mathrm{d}A}, \tag{13}$$

where

$$W_e = \int_S \mathbf{t}_e \cdot \mathbf{u} \, \mathrm{d}S, \quad E_s = \frac{1}{2} \int_V \boldsymbol{\sigma} : \boldsymbol{\varepsilon} \, \mathrm{d}V, \quad E_k = \frac{1}{2} \int_V \rho \frac{\partial \mathbf{u}}{\partial t} \cdot \frac{\partial \mathbf{u}}{\partial t} \mathrm{d}V$$

are the total external work, strain and kinetic energy, respectively, and $\mathbf{t}_e$ is the external traction vector.

4. FLUID–STRUCTURE COUPLING

In the present work, the contained fluid is represented by p_0 ahead of the crack front, while the pressure decay behind the crack tip is predicted by an implicit coupling between a 1-D gas dynamic analysis with the FV numerical model.

The 1-D model begins with the integral form of the mass continuity equation:

$$\frac{\partial}{\partial t} \int_V \rho \, \mathrm{d}V + \int_S \rho \mathbf{v} \cdot \mathbf{n} \, \mathrm{d}S = 0, \tag{14}$$

where ρ is the fluid density and $\mathbf{v}$ is the velocity vector.

In the case of the S4 test we make the following assumptions: (i) ahead of the crack tip, the gas is assumed to be stationary; (ii) behind the crack tip, axial flow is negligible; (iii) within the cross-section, the gas is stationary and pressure decay is solely due to out-flow through the crack opening (Figure 3); the inferred assumption of axial planar flow is supported by the experimental work of Leevers *et al.* (1993) who measured negligible circumferential variation in pressure behind the crack tip in the S4 test.

The continuity equation for the axial "slice" of pipe is

$$A \frac{\partial \rho}{\partial t} + 2\rho_e v_e u_e = 0, \tag{15}$$

where A is the cross-sectional area, ρ the density, t the time, and ρ_e, v_e and $2u_e$ are the density, flow velocity and crack opening at the out-flow exit plane (Figure 3). Flow at the exit plane is sonic, while the pressure p, within the cross-section, is greater than

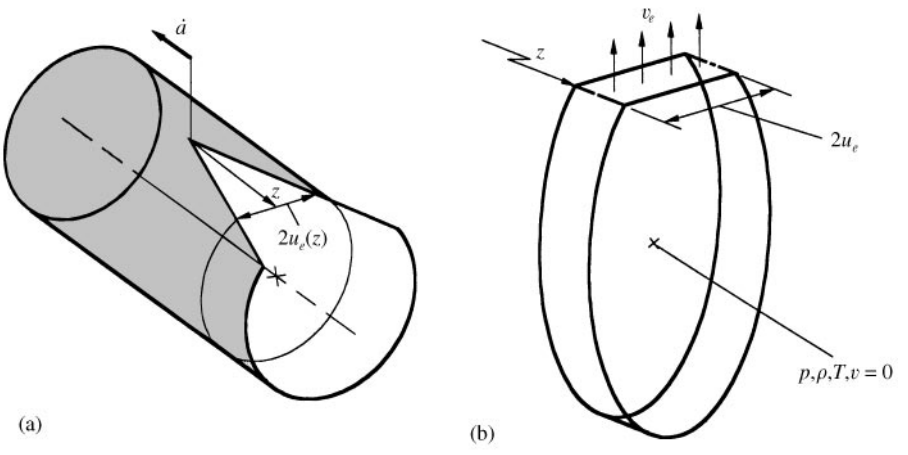

Figure 3. (a) Schematic diagram of pipe RCP; (b) axial "slice" of pipe behind the crack tip.

$p_a(\gamma/2+1/2)^{\gamma(\gamma-1)}$ where p_a is atmospheric pressure. For small crack openings, conditions within the pipe and at the exit plane are related by the well-known equations of choked flow (Liepmann & Roshko 1957), which combined with equation (15) leads to the following expression for pressure decay:

$$\frac{\mathrm{d}p}{\mathrm{d}t} = -\underbrace{\gamma\left(\frac{2}{\gamma+1}\right)^{(\gamma+1)/2(\gamma-1)}\sqrt{\gamma RT}}_{\text{gas constant \& temperature}}\ \underbrace{\frac{4}{\pi}\frac{1}{\eta_A}\left(\frac{D^*}{D^*-2}\right)^2\frac{2u_e}{D^2}}_{\text{cross section \& crack opening}}\ \underbrace{p_0\left(\frac{p}{p_0}\right)^{(3\gamma-1)/2\gamma}}_{\text{pressure}}, \qquad (16)$$

where R is the constant, T is the absolute temperature, $\sqrt{\gamma RT}$ is the speed of sound in the gas, D is the diameter, and $D^* \equiv D/B$. η_A is the air volume fraction within the pipe which is taken here as 0·75, since 25% of the pipe internal volume is occupied by the core, baffles, and spacers in the S4 test.

When p falls below $p_a(\gamma/2+1/2)^{\gamma/(\gamma-1)}$ the pressure at the exit plane falls to atmospheric and the flow becomes subsonic. The mass continuity equation is then

$$\frac{\mathrm{d}p}{\mathrm{d}t} = -\underbrace{\gamma\left(\frac{2}{\gamma-1}\right)^{1/2}\sqrt{\gamma RT}}_{\text{gas constant \& temperature}}\ \underbrace{\frac{4}{\pi}\frac{1}{\eta_A}\left(\frac{D^*}{D^*-2}\right)^2\frac{2u_e}{D^2}}_{\text{cross section \& crack opening}}\ \underbrace{p_t\left(\frac{p}{p_0}\right)^{(3\gamma-1)/2\gamma}\left[\left(\frac{p_a}{p}\right)^{2/\gamma}-\left(\frac{p_a}{p}\right)^{(\gamma+1)/\gamma}\right]^{1/2}}_{\text{pressure}}. \qquad (17)$$

Equations (16, 17) are discretized in time and coupled with the FV stress analysis model to provide the fluid boundary conditions. Taking $\gamma = 1{\cdot}4$ for air, the guage pressure at boundary cell centres within a particular axial cross-section is

$$p^m = p^{m-1} - 2{\cdot}44\delta t\frac{d_p\sqrt{RT_0}}{\eta_A}\frac{p_a}{(p_0/p_a+1)^{1/7}}\left(\frac{p^m}{p_a}+1\right)^{8/7}u_e^m \quad \text{for } p^m > 1{\cdot}89, \qquad (18)$$

$$p^m = p^{m-1} - 9{\cdot}43\delta t\frac{d_p\sqrt{RT_0}}{\eta_A}\frac{p_a}{(p_0/p_a+1)^{1/7}}\sqrt{\left(\frac{p^m}{p_a}+1\right)^{6/7}-\left(\frac{p^m}{p_a}+1\right)^{4/7}}\,u_e^m \quad p^m \le 1{\cdot}89,$$

where $p_a = 10^5$ Pa, $d_p = [D^*/(D^* - 2)]^2/D^2$ and T_0 is the crack tip temperature, specified in the simulations as 295 K. Within each time step, we iterate for u_e and p until the fully implicit coupled solution reaches convergence.

5. MODEL VALIDATION

The coupled FVID-gas model was examined using gas pressure measurements from four piezoelectric transducers located along the core of the S4 test rig (Figure 1). The time delay between the onset of decompression at successive transducers provided an approximate crack history input to the numerical mode. A typical simulation gives results for G, p and crack opening displacement COD as the crack advances through successive diameter lengths of pipe, as shown in Figure 4. Note that the pressure profile is truncated within the anvil zone since there is very little gas in this region (Figure 1). The calculated G is inevitably small here and in practice it is the energy of initiation provided by the striker which drives the crack into the gauge section.

The predicted pressure profiles at each transducer location are compared to the experimental records in Figure 5, although the profiles are clipped when the crack reaches the end of the pipe and the simulation terminates. The slope of pressure decay is solely dependent on the crack opening displacements and the mass out-flow rate, computed by the structural and gas dynamics components of the FVID-gas model, respectively. Therefore, the good overall agreement between prediction and experiment suggests that both the FV structural model of pipe deformation and the 1-D analytical model of gas discharge are very realistic. Any discrepancy at the lower part of the pressure profiles is probably due to pipe wall vibrations behind the crack tip generating pressure waves which the 1-D gas model cannot account for.

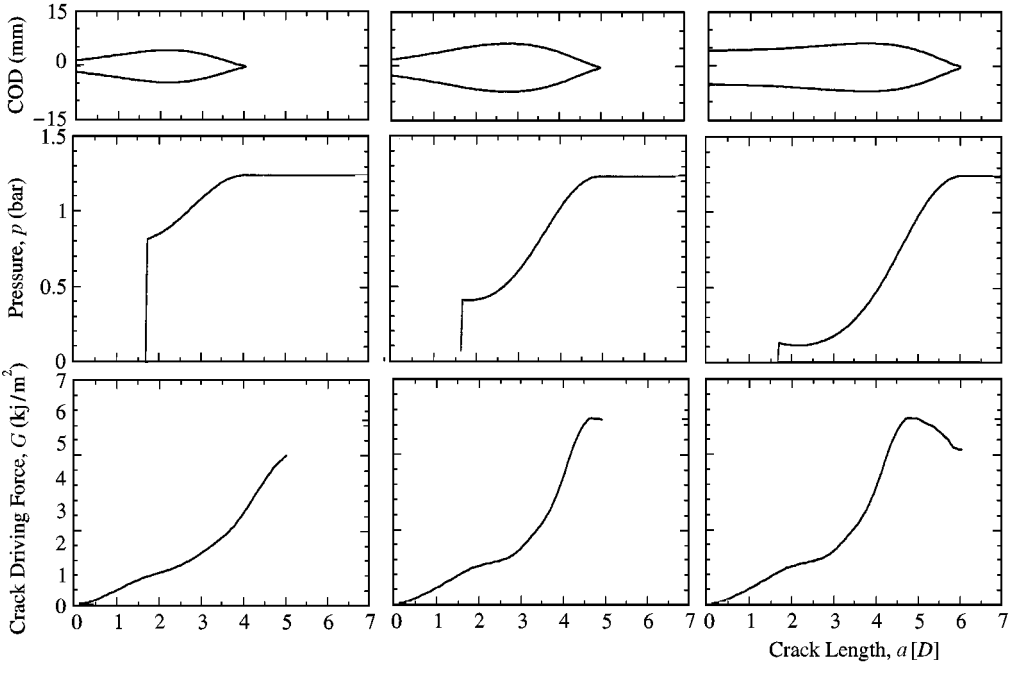

Figure 4. Snapshots of crack opening, pressure and crack driving force (PE80, 250 SDR 11, 0°C, 1·25 bar, $\dot{a} = 175$ m/s).

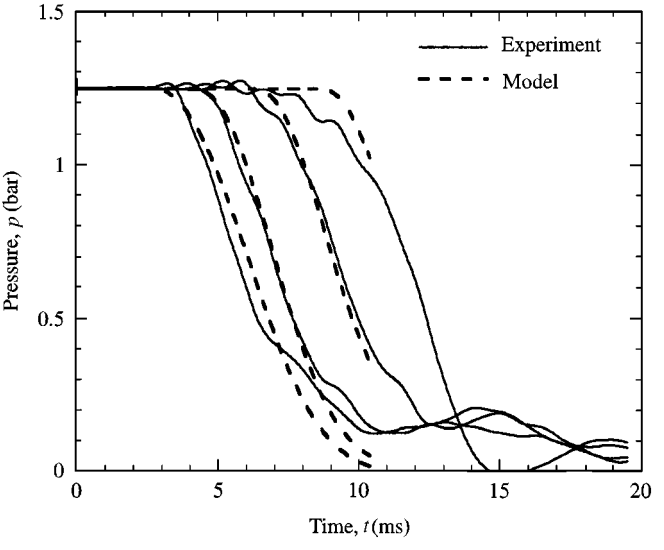

Figure 5. Experimental and predicted pressure profiles (PE80, 250 SDR 11, 0°C, 1·25 bar, $\dot{a} = 175$ m/s).

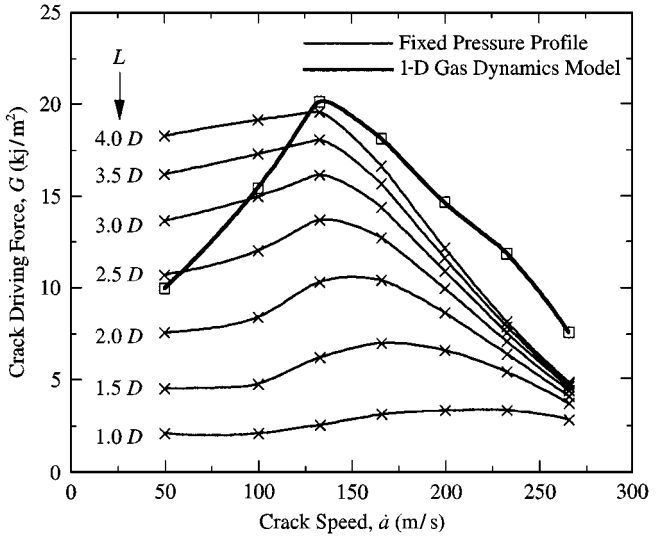

Figure 6. Variation of crack driving force with crack speed: fixed pressure profile versus 1-D gas dynamics model (PE80, 160 SDR 11, 0°C, 4 bar).

6. BENEFITS OF THE FVID-GAS MODEL

In the absence of the 1-D gas model, a pressure discharge profile has to be prescribed in numerical simulations. Ivankovic & Venizelos (1998) previously implemented a linear pressure decay from p_0 and p_a over a specified decompression length L. Several combinations of crack speed $\dot{a}$ and decompression length were used in a set of simulations to obtain a family of curves relating G and $\dot{a}$ (Figure 6). In this and subsequent analyses, the singular value of G represents an average during propagation from a crack length of $4D$ to $6D$. A decompression length could then be extracted from any S4 test pressure records and matched to the numerical simulation to calculate G for the specific test conditions. Using

the model to predict a critical pressure under a different set of test conditions required a prior estimate for the single unknown parameter L.

In contrast, no prior knowledge of the decompression length is required by the 1-D-gas model and thus we obtain a single G versus $\dot{a}$ curve, which is actually the locus of the only possible combinations of crack speed and decompression length. Of course, the 1-D gas model and fixed, linear decompression simulation yield similar G data when the decay profile lengths match one another. The FVID-gas model can be used to predict critical pressures exactly from the material properties and geometry alone. It also vastly reduces the number of simulations required to generate all possible G versus $\dot{a}$ characteristics for a given test case. The example in Figure 6 illustrates a sevenfold reduction from 49 simulations to 7.

7. PARAMETRIC STUDY

Two pipe materials, e.g. PE and PVC-U (unplasticized poly-vinyl-chloride), can exhibit different critical pressures due to differences in fracture toughness, modulus and density. To determine how each individual parameter actually affects the critical pressure would require a large amount of test data from a wide variety of materials. Even after several years of research into gas pipe fracture, the dependence of critical pressure on basic pipe properties and geometry remains ill-defined.

However, the coupled FVID-gas model presents an opportunity to isolate the effect of individual parameters on crack driving force and, hence, on critical pressure. Table 1 shows the input parameters from six sets of S4 test simulations for which the model was executed at constant crack speeds of 50, 100, 133, 166, 200, 233, 266, 300 m/s and at input pressures of 1, 2 and 4 bar. The gas constants in Table 1 were chosen to represent air (287 J/kg K) and a fuel gas (459 J/kg K).

In Figures 7–9, the G versus $\dot{a}$ curves are presented as a single curve for each pressure, both in terms of absolute G and also normalized by G_0 which is the contribution to the driving force provided by the release of strain energy, derived by Irwin & Corten (1968):

$$G_0 = \frac{\pi}{8}\frac{p_0^2}{E}\frac{(D^* - 1)(D^* - 2)^2}{D^*}D, \tag{19}$$

where D^* is the diameter to thickness ratio.

7.1. Effect of Pressure

The effect of pressure on G in the "control" test is shown in Figure 7. The three curves are of similar shape and effectively scale with pressure as $G \propto p^{1{\cdot}8}$, which is broadly in line with the $G \propto p^2$ relationship of equation (19).

Table 1

Numerical test cases for the parameteric study of the S4 test

Test case name	Diameter, D (mm)	Diameter/ thickness ratio, D^*	Dynamic modulus E (GPa)	Density, ρ (kg/m^3)	Gas constant, R (J/kg K)
Control	160	11·0	2·5	940	287
Diameter	**250**	11·0	2·5	940	287
D^*	160	**17·6**	2·5	940	287
Modulus	160	11·0	**4·0**	940	287
Density	160	11·0	2·5	**1520**	287
Gas constant	160	11·0	2·5	940	**459**

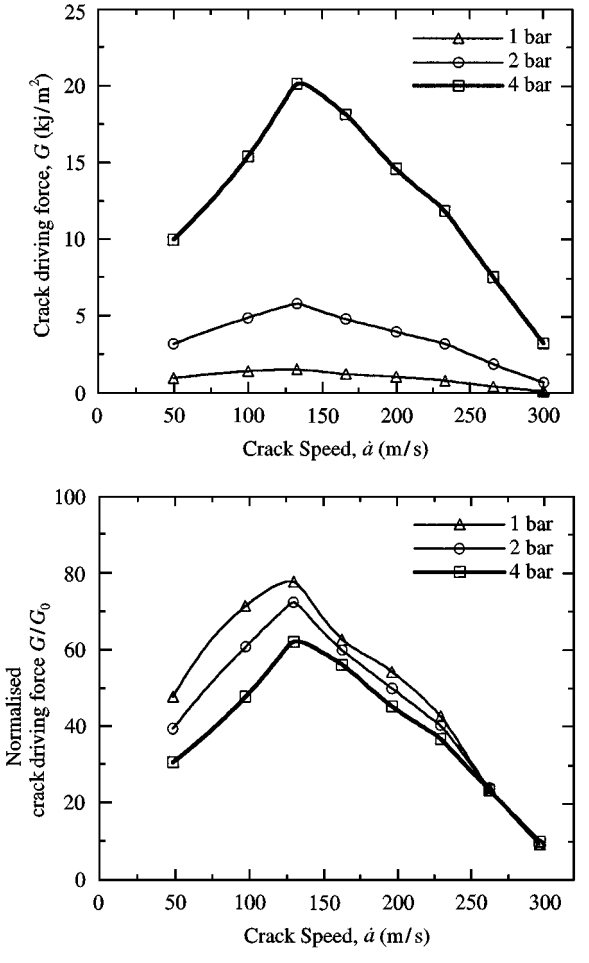

Figure 7. Effect of pressure on crack driving force.

7.2. Effect of Diameter and Thickness

The relationship between G and pipe dimensions is illustrated by the 4 bar pressure simulations, shown in Figure 8. The "control" and "diameter as parameter" curves virtually superimpose when scaled linearly by diameter, i.e., $G \propto D$. A relationship of $G \propto (D^* - 2)^2$, corresponding to higher stresses in thinner pipes, closely correlates with the numerical simulation.

7.3. Effect of Modulus, Density and Gas Constant

The effect of dynamic modulus, E, density, ρ, and gas constant, R, on G is illustrated by the 4 bar pressure simulations shown in Figure 9. The results can be explained by considering that G increases with pressure loading and crack opening. Higher modulus and density manifest themselves as higher pipe wall stiffness and inertia, both restricting the crack opening. The model shows that:

(i) A pipe wall of higher modulus deforms less and generally causes G to decrease. However, at very high speeds, the reduced crack opening generates smaller inertia forces which causes G to increase.

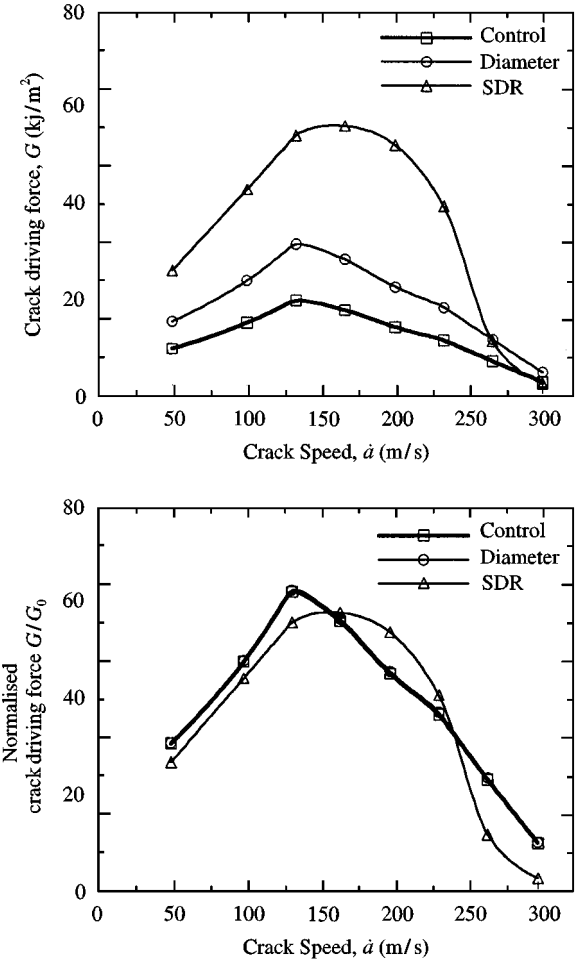

Figure 8. Effect of pipe dimensions on crack driving force.

(ii) As density increases, the effect of inertia at low crack speeds causes a small reduction in maximum G and the crack speed at which it occurs, whereas at high crack speeds, the increased inertia leads to a marked reduction in G.
(iii) A higher gas constant leads to slightly more rapid decompression and hence a small decrease in G.

Although it is difficult to quantify the effect of density and gas constant, the modulus dependency is $G \propto E^{-0{\cdot}7}$. In summary, an approximate relationship between critical pressure and key parameters of RCP is

$$G \propto p_c^{1{\cdot}8} E^{-0{\cdot}7} D(D^* - 2)^2. \tag{20}$$

The Irwin–Corten strain energy analysis, equation (19), yields a similar relationship to this, although it predicts higher nominal values of critical pressure than we measure in a gas-pressurized S4 test because it does not account for the work done by the gas during fracture.

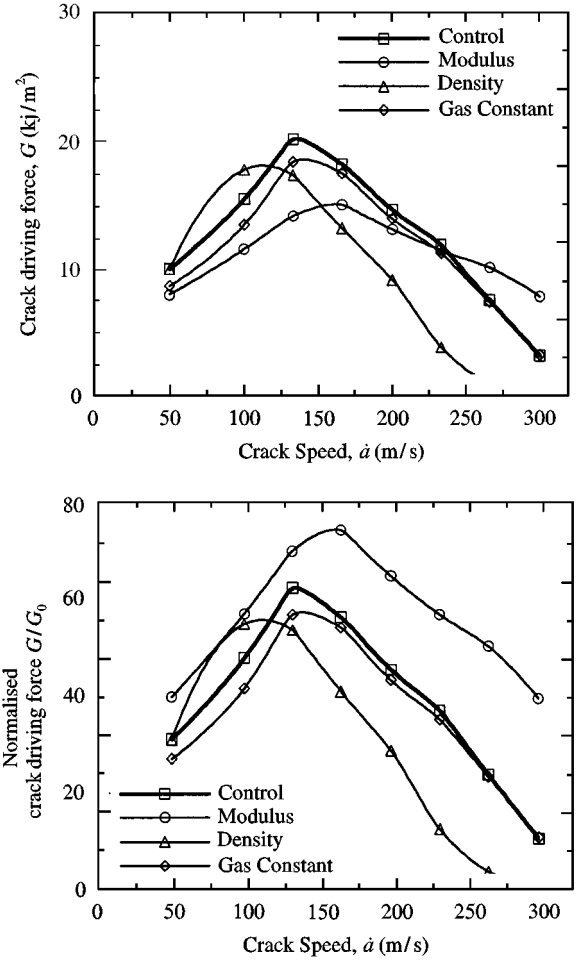

Figure 9. Effect of material and fluid parameters on crack driving force.

8. CONCLUSIONS

We have presented a computational model for rapid crack propagation in the S4 pipe test. The model combines the FV method which simulates the deformation and fracture of the pipe, with a 1-D compressible flow analysis that describes gas discharge through the crack opening. The model predicts gas decompression profiles which are in very good agreement with experimental measurements. The FVID-gas model is more efficient than previous models, where the decompression length had to be assumed, because there is no need to simulate "redundant" combinations of crack speed and decompression length. It has made it possible to determine how key geometric and material parameters affect the crack driving force and thus the critical pressure. This parametric study has produced an empirical relationship by which the gas pipeline industry can understand the effect of some basic parameters on pipe RCP performance. It is particularly useful to be able to scale S4 test results to the highest pipe diameters, which cannot easily be tested at reasonable cost.

References

Greig. J. M. 1996 Rapid crack propagation in polyethylene gas pipes. *Plastic, Rubber and Composites Processing and Applications* **25,** 163–168.

International Standardisation Organisation ISO 13477. 1996 Thermoplastics pipes for the conveyance of fluids—determination of the resistance to rapid crack propagation (RCP)—small-scale steady-state test (S4).

International Standardisation Organisation ISO 13478. 1996 Thermoplastics pipes for the conveyance of fluids—determination of the resistance to rapid crack propagation (RCP)—full-scale test.

Irwin, G. R. & Corten, H. T. 1968 Evaluating the feasibility of basing pipeline operating pressure on in-plane hydrostatic test pressure. Report to Northern Natural Gas Company and El Paso Natural Gas Company, 1968.

Ivankovic, A., Demirdzic, I. & Muzaferija, S. 1997 Finite volume method and multigrid acceleration in modelling of rapid crack propagation in full-scale pipe test. *Computational Mechanics* **20,** 46–52.

Ivankovic, A. & Venizelos, G. P. 1997 Modelling or rapid crack propagation along pressurised plastic pipes. In *Proceedings of the* 10*th International Conference on Deformation, Yield and Fracture of Polymers*, Cambridge, U.K., pp. 526–530.

Ivankovic, A. & Venizelos, G. P. 1998 Rapid crack propagation in plastic pipe: predicting full-scale critical pressure from S4 test results. *Engineering Fracture Mechanics* **59,** 607–622.

Leevers, P. S., Venizelos, G. & Ivankovic, A. 1995 Rapid crack propagation along pressurised PE pipe: small scale test and numerical modelling. *Construction and Building Materials* **7,** 179–184.

Liepmann, H. W. & Roshko, A., 1957. *Elements of Gasdynamics*, pp. 53–54. New York: Wiley.

Nishioka, T 1997 Computational dynamic fracture mechanics. *International Journal of Fracture* **86,** pp. 27–59.

Yayla, P. & Leevers, P. S. 1992 Rapid crack propagation in pressurised plastic pipe—II: critical pressures for polyethylene pipe. *Engineering Fracture Mechanics* **42,** 675–682.